Title

Improved characterization of underground structure defects from two-stage Bayesian inversion using crosshole GPR data

Authors

Qin, Hui
Vrugt, Jasper A
Xie, Xiongyao
et al.

Peer reviewed

Improved characterization of underground structure defects from two-stage Bayesian inversion using crosshole GPR data

Hui Qin[a,b,d,*], Jasper A. Vrugt[d,e], Xiongyao Xie[b,c], Yunxiang Zhou[b,c]

[a] School of Civil Engineering, Dalian University of Technology, Dalian 116024, China
[b] Key Laboratory of Geotechnical & Underground Engineering of Ministry of Education, Tongji University, Shanghai 200092, China
[c] Department of Geotechnical Engineering, Tongji University, Shanghai 200092, China
[d] Department of Civil and Environmental Engineering, University of California Irvine, CA 92697-2175, USA
[e] Department of Earth System Science, University of California Irvine, CA 92697-2175, USA

ARTICLE INFO

ABSTRACT

Crosshole ground-penetrating radar (GPR) is a widely used measurement technique to help inspect the structural integrity of man-made underground structures. In a previous paper, we have introduced a Bayesian framework for inversion of crosshole GPR experiments to help back out defects in concrete underground structures. Here, we evaluate the practical usefulness of our inversion framework by application to waveform data from a real-world GPR survey of a diaphragm wall panel with two embedded structure defects. We also use this case study to further refine our methodology by introducing the elements of a two-stage inversion method to help delineate the exact location and shape of small structure defects. Herein, a low-resolution inversion composed of relatively few inversion coefficients (stage-1) is used to determine roughly the presence of structure defects, followed by a second inversion (stage-2) with much enhanced spatial resolution in those areas classified with anomalous or suspicious permittivity values. This two-stage inversion approach uses more wisely CPU-resources by focusing primarily on those areas of the concrete structure that have been classified as anomalies. We investigate the benefits of this two-stage inversion scheme using a synthetic and real-world case study involving waveform data of a diaphragm wall panel measured with crosshole GPR. Our results demonstrate that the proposed two-stage inversion method recovers successfully the location and shape of structure defects, at a computational cost that is considerably lower than the original inversion framework.

1. Introduction

Ground-penetrating radar (GPR) is a widely used measurement technique to measure the properties of the subsurface and evaluate the integrity of civil structures [1-5]. This method emits high-frequency electromagnetic (EM) waves in the range of 10 MHz to 1 GHz from a transmitter antenna, and these waves are subsequently received by a nearby antenna. When the EM wave encounters an anomaly (buried object) or a boundary between two materials with contrasting dielectric properties, it will be reflected, refracted or scattered back. The signal (waveform) that arrives at the receiver antenna thus stores important information about the structure and properties of the domain in-between the two antennas. For underground structures such as pile foundations and diaphragm walls, defects (e.g. cracks, voids, and weakness zones) may appear during construction and compromise structural integrity and safety [6]. Such structures usually extend up to 30–50 m below the ground surface, which make surface GPR methods

rather ineffective, because the emitted high frequency EM waves do not penetrate sufficiently deep to characterize accurately the underground structure[7]. Fortunately, crosshole GPR extends the ability of surface GPR to deep subsurface media by placing the transmitter and receiver antenna next to each other in the underground structure in two adjacent boreholes several meters spaced apart [8,9]. This allows for a rapid characterization of the EM properties of the structure in-between the two boreholes, commonly referred to as the dielectric permittivity, ε and electrical conductivity, σ [10]. In the case of man-made underground structures, concrete defects are easily infiltrated by ground water, thereby leading to anomalies in the measured ε values [11,12]. Indeed, the dielectric permittivity is a good proxy for the distribution and amount of (soil) water in underground structures.

Ray based methods such as first-arrival traveltime and first-cycle amplitude tomography have found wide application and use to derive ε and σ from crosshole GPR data [13-15]. These approaches exhibit affordable modeling errors and have the advantage of being relatively

---

CPU-efficient [16-18], yet their resolution is limited to the scale (diameter) of the first Fresnel zone [19,20]. Consequently, these methods can only resolve features larger than the dominant signal wavelength. Full-waveform inversion, on the contrary, allows for a much more detailed characterization (sub-wavelength resolution) by solving numerically Maxwell's equations in two- or three-spatial dimensions using the exact geometry, physical parameters, boundary conditions, excitation, time step, and transmitter and receiver positions of the actual GPR experiment [21,22]. This approach has enjoyed a lot of attention in the past few years [23-31] but the forward model (e.g. Maxwell's equations) and inverse solution place a heavy burden on computational resources. This can be alleviated somewhat if the inversion is limited only to inference of the "best" permittivity distribution of the structure of interest. This realization exhibits the closest match between the observed and simulated EM waves but does not appropriately communicate measurement and modeling uncertainties [32]. Probabilistic inversion methods allow for the treatment of different sources of error and return to the user an ensemble of realizations deemed statistically acceptable [33-40]. Among these methods, Bayesian inference coupled with Markov chain Monte Carlo (MCMC) simulation has found widespread application and use in GPR inversion.

In a previous paper, we have developed a Bayesian inversion methodology to infer the relative permittivity distribution, ε_r of underground structures from crosshole GPR waveform data [41]. The relative permittivity is related to the permittivity as follows, $\varepsilon_r = \varepsilon/\varepsilon_0$, where ε_0 denotes the free space dielectric permittivity. Our method uses as main building blocks two-dimensional finite-difference time-domain (FDTD) simulation [42,43], the discrete cosine transform (DCT) [44,45], and Markov chain Monte Carlo (MCMC) simulation with the differential evolution adaptive Metropolis algorithm (DREAM$_{(ZS)}$) [46-49], and thus is coined FDTD-DCT-DREAM$_{(ZS)}$ framework. The FDTD simulator solves numerically Maxwell's equations in the time and space domain of the crosshole GPR experiment and simulates iteratively the EM waveforms. The DCT algorithm transforms the Cartesian parameterization to the frequency domain and reduces drastically the dimensionality of the parameter space by retaining only the lower-frequency DCT-coefficients. MCMC simulation with the DREAM$_{(ZS)}$ algorithm is used to estimate the posterior distribution of the DCT-coefficients. Numerical experiments with synthetic waveform data were used by [41] to demonstrate the ability of the FDTD-DCT-DREAM$_{(ZS)}$ framework to successfully back out structure defects. Indeed, the DCT approach sacrifices model resolution and may not recover correctly with sufficient fidelity structure defects, particularly if these anomalous areas appear relatively small in comparison to the surrounding structure. A simple remedy to this problem would be to use a much larger number of DCT-coefficients, yet at the expense of a significant increase in the computational requirements of the FDTD-DCT-DREAM$_{(ZS)}$ framework.

In this paper, we evaluate the practical applicability of the FDTD-DCT-DREAM$_{(ZS)}$ framework using measured waveform data from a crosshole GPR survey of a diaphragm wall model with embedded structure defects. We also introduce in this paper an alternative two-stage inversion method, wherein a rather simple inversion with relatively few DCT-coefficients is used to determine roughly the presence of structure defects, followed by a second inversion with much enhanced resolution in those areas of the concrete body that were identified as anomalous or suspicious in the first inversion. We illustrate this two-stage approach by application to artificial data from a synthetic GPR experiment, and the measured waveforms of the diaphragm wall model. In both studies, we are especially concerned with the computational efficiency of our method, and investigate the relationship between the number of DCT-coefficients that is used to characterize the relative permittivity values of the concrete structure, and the corresponding CPU-costs of the DREAM$_{(ZS)}$ algorithm. This paper concludes with a summary of the main findings.

2. Methodology

In the following subsections we will describe the different elements of our Bayesian inversion framework to help detect defects in manmade underground structures.

2.1. FDTD-DCT-DREAM$_{(ZS)}$ inversion framework

We have recently developed a Bayesian waveform inversion strategy to infer the relative permittivity field of underground concrete structures. This inversion method combines two-dimensional FDTD solution of the Maxwell's equations, parameter dimensionality reduction with the DCT, and the DREAM$_{(ZS)}$ algorithm to facilitate a rapid and efficient characterization of the relative permittivity distribution of the underground structure of interest. A detailed description of this method appears in [41] and so will not be repeated herein. Instead, we only briefly summarize the main building blocks of this framework.

In crosshole GPR, an EM pulse, $\widetilde{\mathbf{u}}$, is emitted by a transmitter antenna in one borehole, and the resulting waveform, $\widetilde{\mathbf{y}} = \{\widetilde{y}_1, ...,\widetilde{y}_N\}$, which consists of N data points measured by a receiver antenna in an adjacent borehole spaced several meters apart. By using multiple different vertical positions of the transmitter and receiver antennas a data set of n waveforms is obtained which contains detailed information about the physical properties of the underground structure in-between the two boreholes. For a single position of the transmitter and receiver antenna, the GPR experiment can be described as follows

$$\widetilde{\mathbf{y}} = f(\mathbf{m}, \widetilde{\mathbf{u}}) + \mathbf{e}, \tag{1}$$

where $\mathbf{m}$ is a d-vector of model parameters that describes the physical properties of the subsurface structure, $f(\cdot)$ denotes the forward model which simulates the physical relation between $\mathbf{m}$, $\widetilde{\mathbf{u}}$, and $\widetilde{\mathbf{y}}$, and $\mathbf{e} = \{e_1,...,e_N\}$ is a N-vector of error residuals that lumps together waveform measurement data errors, model structural and input data errors. In this study, the d-vector $\mathbf{m}$, characterizes the relative permittivity distribution of the underground structure wherein defects appear as local anomalies. The function, $f(\cdot)$, used herein is equivalent to the FDTD model which describes numerically the EM wave propagation between the transmitter and receiver antennas using numerical solution of Maxwell's equations [42,43]. The tilde operator, $\widetilde{}$ is used to denote measured quantities. We solve Eq. (1) for the n different transmitter and receiver antenna positions used in the GPR experiment, and store the simulated waveforms of N data points in the $n \times N$-matrix, $\widetilde{\mathbf{Y}}$.

The model parameters, $\mathbf{m}$ cannot be derived from closed-form analytic solutions, and we therefore have to resort to iterative methods to determine the relative permittivity distribution from the measured waveform data, $\widetilde{\mathbf{Y}}$. We adopt herein a probabilistic inversion method and derive the posterior probability distribution of the parameters, $p(\mathbf{m}|\widetilde{\mathbf{Y}})$ using Bayes theorem

$$p(\mathbf{m}|\widetilde{\mathbf{Y}}) = \frac{p(\mathbf{m})p(\widetilde{\mathbf{Y}}|\mathbf{m})}{p(\widetilde{\mathbf{Y}})}, \tag{2}$$

where $p(\mathbf{m})$ denotes the prior distribution and summarizes all probabilistic knowledge of $\mathbf{m}$ before collecting the GPR data set, $L(\mathbf{m}|\widetilde{\mathbf{Y}}) \equiv p(\widetilde{\mathbf{Y}}|\mathbf{m})$ signifies the likelihood function, and $p(\widetilde{\mathbf{Y}})$ is equivalent to a normalization constant, also called marginal likelihood or evidence, which ensures that the posterior distribution integrates to unity. In practice, we often discard, $p(\widetilde{\mathbf{Y}})$, and draw all our inferences from the unnormalized density

$$p(\mathbf{m}|\widetilde{\mathbf{Y}}) \propto p(\mathbf{m})L(\mathbf{m}|\widetilde{\mathbf{Y}}). \tag{3}$$

The likelihood function, $L(\mathbf{m}|\widetilde{\mathbf{Y}})$, quantifies in probabilistic terms, the (dis)agreement between the observed and FDTD simulated GPR waveforms. If we assume the measurement data errors of the GPR waveforms, $\widetilde{\mathbf{Y}}$, to be independent and Gaussian distributed, the log-likelihood function, $\mathscr{L}(\mathbf{m}|\widetilde{\mathbf{Y}})$ is relatively easy to derive and equivalent

to

$$\mathscr{L}(\mathbf{m}|\widetilde{\mathbf{Y}}, \hat{\sigma}^2) = -\frac{T}{2}\ln(2\pi) - \frac{T}{2}\ln(\hat{\sigma}^2) - \frac{1}{2}\hat{\sigma}^{-2}\sum_{i=1}^{T}(f_i(\mathbf{m}) - \widetilde{Y}_i)^2,$$
(4)

where $\hat{\sigma}^2$ is a nuisance variable that signifies the variance of the measurement data error, and $T = n \times N$ represents the total number of GPR observations, and the counter i denotes the element (index) of the matrix $\widetilde{\mathbf{Y}}$. In the absence of detailed information about the measurement data error, we can approximate $\hat{\sigma}^2$ with a "sufficient" statistic, $s^2 = \frac{1}{T-1}\sum_{i=1}^{T}(f_i(\mathbf{m}) - \widetilde{Y}_i)^2$, which, after some rearrangement, leads to the following definition of the log-likelihood function

$$\mathscr{L}(\mathbf{m}|\widetilde{\mathbf{Y}}) \propto -\frac{T}{2}\ln\left(\sum_{i=1}^{T}(f_i(\mathbf{m}) - \widetilde{Y}_i)^2\right).$$
(5)

The proportionality sign replaces the equality sign in Eq. (4) because all constant terms independent of the parameters, $\mathbf{m}$, have been removed. This does not affect the maximum likelihood values of the parameters, nor their marginal and joint posterior distribution, as all statistical inferences of $\mathbf{m}$ are made from the differences in the log-likelihoods. Note, the sum of these canceled terms is equivalent to the natural logarithm of the normalization constant, which guarantees that the conditional distribution, or likelihood function, integrates to unity. The latter is a requirement for Bayesian model selection to determine the "best" model among an ensemble of competing hypotheses.

In this work, we use MCMC simulation with the DREAM$_{(ZS)}$ algorithm to generate samples from the posterior distribution, $p(\mathbf{m}|\widetilde{\mathbf{Y}})$. This method runs K different chains simultaneously and proposals are generated on the fly from the collection of samples states using parallel direction and snooker sampling. This approach automatically tunes the scale and orientation of the proposal distribution and therefore leads to high sampling efficiencies and a relatively rapid convergence to the target distribution. Details of the DREAM$_{(ZS)}$ algorithm can be found in [47-49] and interested readers are referred to these publications for further details.

The d-vector $\mathbf{m}$ with parameter values sampled by the DREAM$_{(ZS)}$ algorithm characterizes the relative permittivity distribution of the underground structure of interest. If we were to use a uniform parameterization then the inference would involve many thousands to millions of unknowns, namely the relative permittivity of each individual grid cell. The use of such Cartesian parameterization has the key advantage of providing a localized and uniform spatial resolution, yet the resulting inversion problem is prohibitively difficult to solve as it requires the estimation of a very large number of unknowns. What is more, the use of discrete boundaries between permittivity values of neighboring cells not only can complicate forward simulation, but also lead to visually suspect inversion results. We therefore resort to an alternative parameterization approach and use the DCT method to map the spatial parameters to the frequency domain. Then we can safely discard the higher-frequency DCT-coefficients without losing important information about the spatial distribution of the relative permittivity values. Those lower-frequency DCT-coefficients are retained and define a sparse parameterization that will be estimated using the DREAM$_{(ZS)}$ algorithm. This approach significantly reduces the dimensionality of the search space [39,40,45], and improves drastically the computational efficiency of the numerical inversion.

2.2. Two-stage inversion method

The DCT approach reduces significantly the dimensionality of the search space, thereby improving considerably the computational efficiency of the inference, but possibly at the expense of an insufficient model resolution required to delineate and demarcate sharply structure defects. Indeed, truncation of the higher-frequency DCT-coefficients can sacrifice the necessary model resolution required to characterize accurately the location and shape of structure defects. Of course, we can

easily enhance the resolution of the resolved relative permittivity distribution by increasing drastically the number of DCT-coefficients subject to inference. This approach not only frustrates the effectiveness of the dimensionality reduction approach but also decreases considerably the CPU-efficiency of the FDTD-DCT-DREAM$_{(ZS)}$ framework.

We propose herein a simple refinement of the FDTD-DCT-DREAM$_{(ZS)}$ framework of [41] which guarantees a sufficient spatial detail of the structure defects at reasonable computational cost. This alternative implementation uses a two-stage approach, where in the first step only a sufficient number of lower-order DCT-coefficients is used to detect the presence of areas with anomalous permittivity values, followed by a second step in which the spatial resolution of the model is enhanced significantly in these anomalous areas to delineate exactly the location and shape of each structure defect. These anomalous areas are hereafter also referred to as areas of interest, abbreviated AOIs. In the second inversion, we fix the relative permittivity values outside the AOIs to their posterior mean values derived from the first inversion. This first step is also conveniently referred to hereafter as full-domain inversion.

To determine the number of retained DCT-coefficients, or the cut-off frequency of the DCT approach, is a trade-off between spatial resolution and computational expense. We herein use a synthetic example to illustrate the basic principle of the truncation criterion.

First and foremost, the minimum size of target that we expect to resolve needs to be determined before applying parameterization. Note that the full-waveform inversion of crosshole GPR data has the resolution limit up to half the dominant signal wavelength [21], which means any feature less than this scale will be ignored. Therefore in the first step the choice of the number of lower-frequency DCT-coefficients should ensure that the reduced-order DCT representation is capable of revealing the presence of possible defects with minimum resolvable size. For instance, suppose we employ a crosshole GPR system with dominant frequency, $f_m = 450$ MHz to work in an underground structure with relative permittivity, $\varepsilon_r = 12$. Then the dominant wavelength, λ_m can be calculated as $\lambda_m = v/f_m = (c/\sqrt{\varepsilon_r})/f_m = 0.2$ m, where v and c denote the EM wave velocities in the underground structure and vacuum, respectively. Thus the minimum length that can be resolved by the crosshole GPR measurement with full-waveform inversion is $L_{min} = \lambda_m/2 = 0.1$ m.

We now create a synthetic unit square ε_r field with grid size of 0.02 m $\times$ 0.02 m as the reference model (see Fig. 1a), in which a 0.1 m $\times$ 0.1 m (half wavelength) square-shaped defect is simulated using $\varepsilon_r = 16$, higher than $\varepsilon_r = 12$ for the surrounding medium. Note that in real cases the synthetic model dimension and grid size should be the same as those of the forward model in the FDTD-DCT-DREAM$_{(ZS)}$ framework. Next, we transform the reference matrix into the frequency domain using DCT and reconstruct the ε_r field with different numbers of lower-order DCT-coefficients. Fig. 1 b to f presents the reconstructed ε_r fields using $d =$ (b) 64, (c) 100, (d) 144, (e) 196 and (f) 256 DCT-coefficients, respectively. It is obvious that as the number of retained DCT-coefficients increases, the reconstructed ε_r field resolves better the defect. In Fig. 1 b ($d = 64$) and c ($d = 100$), a blurred higher ε_r area in the center of the reconstructed model can be noticed that indicates the presence of the defect. In Fig. 1d, the use of $d = 144$ DCT-coefficients reproduces a much more clear higher ε_r area, providing us better confidence of the presence of the defect. When this number further increases to $d = 196$ (Fig. 1e) and 256 (Fig. 1f), the defect area becomes sharper and more concentrated. By visual inspection of the reconstructed ε_r fields, the choice of $d = 144$ DCT-coefficients is appropriate for the first inversion step as it indicates strongly the presence of the defect while remains a relatively small number. As for the second step, a larger proportion of DCT-coefficients is needed to recover more spatial details, while this number should be also computationally affordable.

In order to quantify the determination of the number of DCT-coefficients, we plot in Fig. 1g the correlation coefficients between the
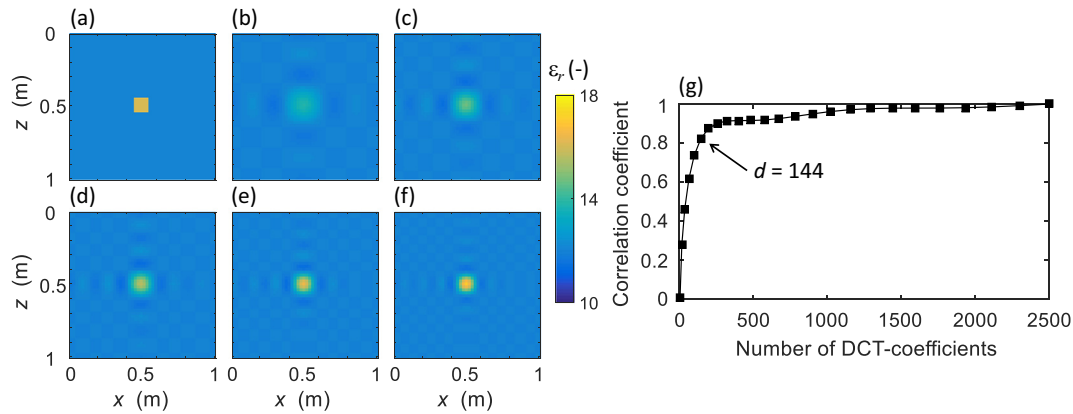
Fig. 1. Determination of the retained number of DCT-coefficients using a synthetic ε_r model: (a) Reference ε_r field, (b–f) reconstructed ε_r fields using (b) $d = 64$, (c) $d = 100$, (d) $d = 144$, (e) $d = 196$, and (f) $d = 256$ DCT-coefficients, and (g) correlation coefficients between the reference model and reconstructed ε_r fields using different numbers of DCT-coefficients.

reference model and its reduced order DCT representations. The correlation coefficient increases rapidly to 0.82 as the number of DCT-coefficients reaches 144, and then goes up slowly to 1.0 until the number approaches the full parameter domain. The marginal increase demonstrates that the added benefit of additional DCT-coefficients beyond $d = 144$ is very limited to improve the reconstructed ε_r field. This analysis confirms our findings in the previous visual inspection that the use of $d = 144$ DCT-coefficients reveals the presence of the defect, and more DCT-coefficients improve only spatial details. Therefore, the appropriate number of DCT-coefficients, $d = 144$ for this example, can be selected at the end of the sharp increase period of the correlation coefficient curve. To sum up, the number of lower-frequency DCT-coefficients can be determined by investigating a synthetic ε_r model with minimum resolvable target using visual inspection and correlation analysis of reduced-order DCT representations.

3. Real-world application of FDTD-DCT-DREAM_(ZS) framework

Numerical examples have proven the usefulness and applicability of the FDTD-DCT-DREAM_(ZS) framework in our previous work [41]. We now evaluate the merits of this inversion method by application to waveform data measured by crosshole GPR in a field diaphragm wall model experiment. We first describe the actual experiment and data acquisition, followed by a detailed description of our experiment results and findings.

3.1. Diaphragm wall model and data acquisition

We built a reinforced concrete diaphragm wall model below the ground surface at an experimental site in Shanghai, China. The experimental structure is 3.0 m wide (x direction), 5.0 m long (y direction), and 4.0 m deep (z direction), and is made up of four concrete walls with thickness of 0.35 m (see Fig. 2a). Inside the front facing wall, two 60 mm wide vertical boreholes are drilled spaced 1.5 m apart. At a depth of 2.0 m in the front wall, two cube-shaped defects, coined A and B, are created with edge lengths of 0.25 m and 0.15 m, respectively. These defects are clearly visible in Fig. 2, and consist of a mix of concrete and soil, reminiscent of construction deficiencies in material composition.

After the concrete structure was finalized, a stepped-frequency crosshole GPR experiment was carried out using a vector network analyzer (VNA), a dipole transmitter and receiver antenna with frequency band from 210 to 560 MHz in the left and right-borehole, respectively, and a computer for radar system control and data storage. Further details on the hardware and experiment setup can be found in [50]. In summary, the generator of the VNA creates an EM signal (radar

wave) which is emitted through a coaxial cable to the transmitter antenna in the left borehole, and radiated into the surrounding (underground) material. The resulting signal travels through the concrete structure, and is captured by the receiver antenna in the right borehole. The retrieval is then transmitted to the VNA receiver by a coaxial cable for measurement in the frequency domain. The measured data points are subsequently stored on the computer. Stepped-frequency measurements were made in the range from 100 to 800 MHz using many different depths for the transmitter (T) and receiver (R) antennas. These antenna depths are spaced 0.1 m apart and are marked with red dots (T) and black crosses (R), in the left and right borehole, respectively (see Fig. 2b). Each waveform measured by the VNA consisted of 101 data points.

To maximize information retrieval from the diaphragm wall model, we perform two separate GPR-experiments and collect data using zero-offset profiling (ZOP) and multi-offset gathers (MOG). Both these methods require two closely spaced and parallel boreholes. In ZOP, the transmitter and receiver antennas are aligned horizontally and lowered vertically in tandem to common measurement depths in the two boreholes. To maintain a zero-offset of the transmitter and receiver antennas, the maximum measurement depth is equivalent to the location of the bottom red dot in the left borehole ($z = 3.6$ m). MOG, on the contrary, does not impose restrictions on the alignment of the transmitter and receiver antennas. Instead, the two antennas are allowed to move independently of each other. This measurement approach increases drastically the number of antenna pairs ($27 \times 30 = 810$ transmitter-receiver combinations) that can be measured, thereby enhancing considerably information extraction from the concrete structure of interest.

We present in Fig. 3 the ZOP data (in time domain) and project the measured waveform of each observation depth onto the front-facing concrete wall. The depth that is used to portray each waveform aligns exactly with the vertical position of the transmitter-receiver antenna pair. The ZOP data lack the spatial resolution and information deemed necessary to recover adequately the main features of the material (dielectric) properties of the concrete structure. Nevertheless, the zero-offset waveforms are relatively easy to acquire and interpret, and therefore serve as a preliminary investigation into the presence of structure defects. In Fig. 3a, most of the traces appear rather similar, with the exception of those measured at a depth of 1.9, 2.0, and 2.1 m that are plotted in red. The functional shape of these traces differs substantially from the waveforms measured immediately above and below this zone. Indeed, the aberrant traces exhibit a (somewhat) delayed first-arrival traveltime and much lower amplitude than their counterparts plotted at all the other measurement depths (see Figs. 3b and 3c). These findings suggest the presence of one or more objects with
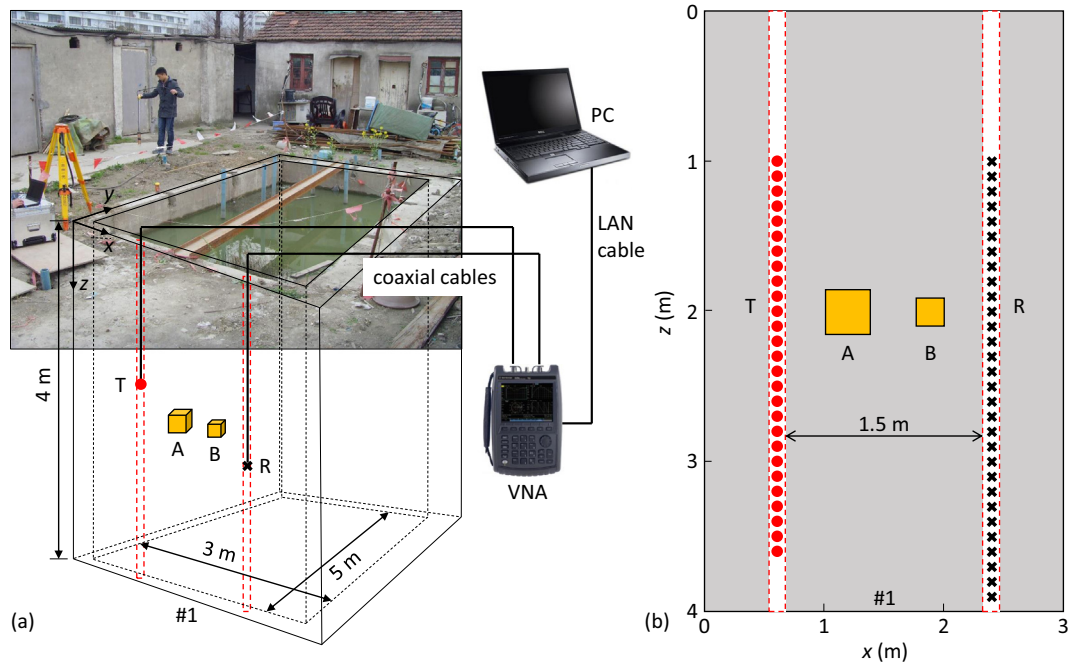
Fig. 2. (a) Overview of the experimental site and concrete underground structure used in our stepped-frequency crosshole GPR-experiment, and (b) crosshole GPR survey configurations. The two cube-shaped items (A and B) consist of a mix of concrete and soil, and serve as structure defects in our analysis. The red dots and black crosses signify the depths of the transmitter and receiver antennas, respectively, that are used to characterize the material properties of the concrete structure.

permittivity much larger than that of the surrounding concrete matrix. Based on these preliminary findings, we can now simplify our analysis by focusing only on a selected portion of the concrete wall between 1.0 and 2.5 m depth which encloses the area of the three aberrant traces.

3.2. Inversion result

We now use the FDTD-DCT-DREAM$_{(ZS)}$ framework to recover the ε_r values of the concrete wall from MOG data. We use the 2D-FDTD model with a regular grid consisting of square cells of 0.02×0.02 m to solve Maxwell's equations for the selected 1.5×1.5 m portion of the concrete wall. We characterize the relative permittivity values of the

$75 \times 75 = 5625$ nodes using $d = 14 \times 14 = 196$ DCT-coefficients and sample the DCT-coefficients in the logarithmic ($\log_{10}$) space using MCMC simulation with the DREAM$_{(ZS)}$ algorithm. We calculate the posterior density of each parameter vector, **m**, using a bounded Jeffreys' prior [51] equivalent to $p(\mathbf{m}) = \mathscr{U}_d[\log_{10}(10), \log_{10}(20)]$ and implement the likelihood function of Eq. (5), where $\mathscr{U}_d[a, b]$ denotes the d-variate uniform distribution with lower and upper bound equal to a and b, respectively.

The DREAM$_{(ZS)}$ algorithm is executed with $K = 4$ different chains using default settings of the algorithmic variables [49]. To maximize computational efficiency, the proposals of each chain are evaluated simultaneously in parallel on four different processors (nodes) using the
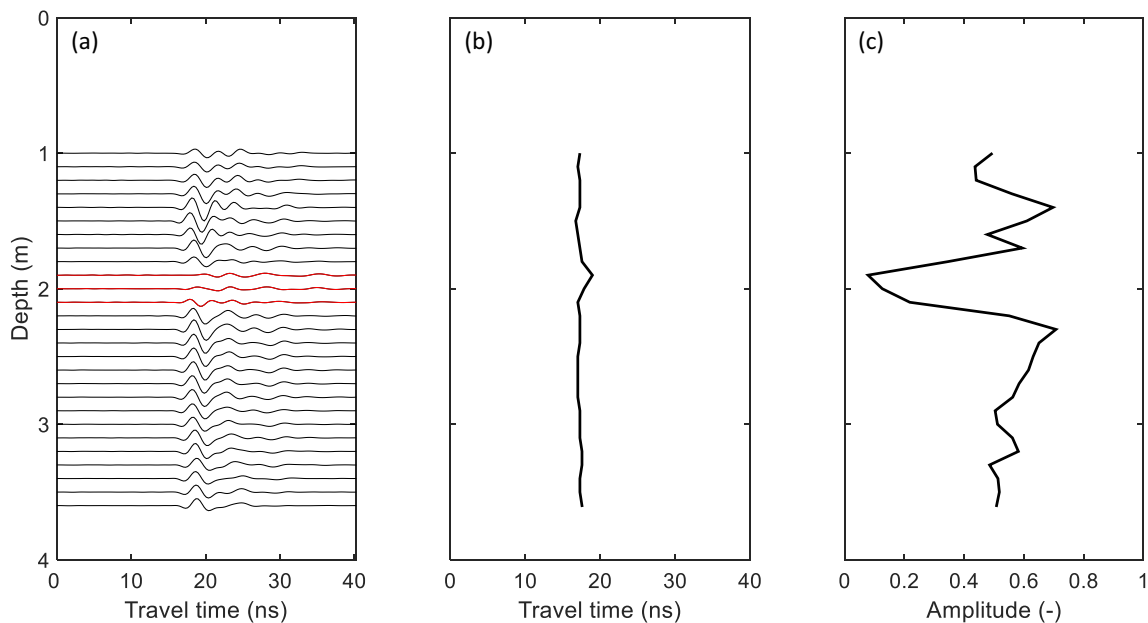

Fig. 3. Measured zero-offset profiling (ZOP) data: (a) ZOP waveforms, (b) first-arrival travel times, and (c) first-cycle amplitudes.

distributed computing toolbox of MATLAB. This multi-core implementation results in an almost linear speed-up of DREAM$_{(ZS)}$ for computationally demanding models such as 2D-FDTD, thereby reducing the required CPU-time to reach convergence to a limiting distribution to about 1/4 of that of a serial implementation of the algorithm. What is more, to enhance the acceptance rate of proposals, the number of crossover values, n_{CR}, and scaling factor of the jump rate, β_0, are set to 20 and 0.25, respectively.

The toolbox of DREAM$_{(ZS)}$ includes various non-parametric and parametric tests to determine when convergence of the sampled chain trajectories to a limiting distribution has been achieved. We use herein the multi-chain $\hat{R}$-statistic of [52] which compares for each parameter the within-chain and between-chain variance. We compute this convergence diagnostic using the last 50% of the sampled values in each chain. To officially declare convergence, the value of $\hat{R}_j \leq 1.2$ for each parameter, $j = \{1,\dots,d\}$. Once convergence is achieved, we use the last 50% of each chain to summarize model parameter and predictive uncertainty.

We summarize the CPU budget of the inversion using the computational time unit (CTU) diagnostic introduced by [38]. We deliberately use this metric as it is independent of the clock-speed of the processors. One CTU is simply equivalent to one generation of the DREAM$_{(ZS)}$ algorithm, or K distributed model evaluations of the 2D-FDTD model. The actual CPU-time (in seconds) scales linearly with the number of CTUs, that is, CPU = αCTU, where α signifies the average time it takes for the processors to complete a single 2D-FDTD model evaluation. In this case, a computational budget of about 164,000 CTUs (1 CTU = 5.11 s) is needed to reach convergence with the DREAM$_{(ZS)}$ algorithm to the posterior distribution of the $d = 196$ DCT-coefficients.

Before we proceed with the results of full-waveform inversion of the MOG data, we first present in Fig. 4a the relative permittivity field of the concrete wall recovered by ray tomography. Transmitter and receiver antenna positions are also marked in this plot with red dots and black crosses, respectively. This approach uses the first-arrival traveltime data only, and therefore leads to a rather poor characterization

with poor resolution, and inaccurate size and shape of the two structure defects. Nevertheless, the measured traveltime data contain sufficient information to detect the presence of two anomalous objects in the concrete wall.

Now we present the results of our FDTD-DCT-DREAM$_{(ZS)}$ framework. The posterior mean ε_r field (Fig. 4b) portrays clearly the presence of two objects, spaced 75 cm apart, with much higher permittivity than the surrounding concrete matrix. The location of these two objects is in excellent agreement with the position of structure defect A and B in the concrete wall. Yet, the resolution of the image is insufficient to warrant a highly detailed characterization of the boundaries and shapes of both defects. The two defects appear oval, whereas a cube-shaped mix of concrete and soil was used in the wall. The associated variance (Fig. 4c) reveals the uncertainty of the ε_r value at each spatial location. We also select three parameters at different locations 1, 2, and 3 marked with "*" in Fig. 4b, and plot their marginal prior (blue) and posterior (red) histograms in in Fig. 4 d to 4f. Notice that the posterior distributions are noticeably more refined than the priors, which indicates that the waveform data contain important information regarding the subsurface ε_r parameters.

4. Case studies of two-stage inversion approach

To illustrate the various elements of our two-stage inversion approach, we first carry out a numerical experiment with known locations of the structure defects, then proceed with the real-world data gathered in the previous field experiment.

4.1. Case study I: numerical experiment

We consider a unit square concrete structure that is buried in the ground. The relative permittivity field, ε_r of this structure is shown in Fig. 5a, and defines our synthetic truth. The concrete is of homogeneous composition, and thus has a constant relative permittivity with the exception of the two defect areas marked with the letters A (0.2 m ×
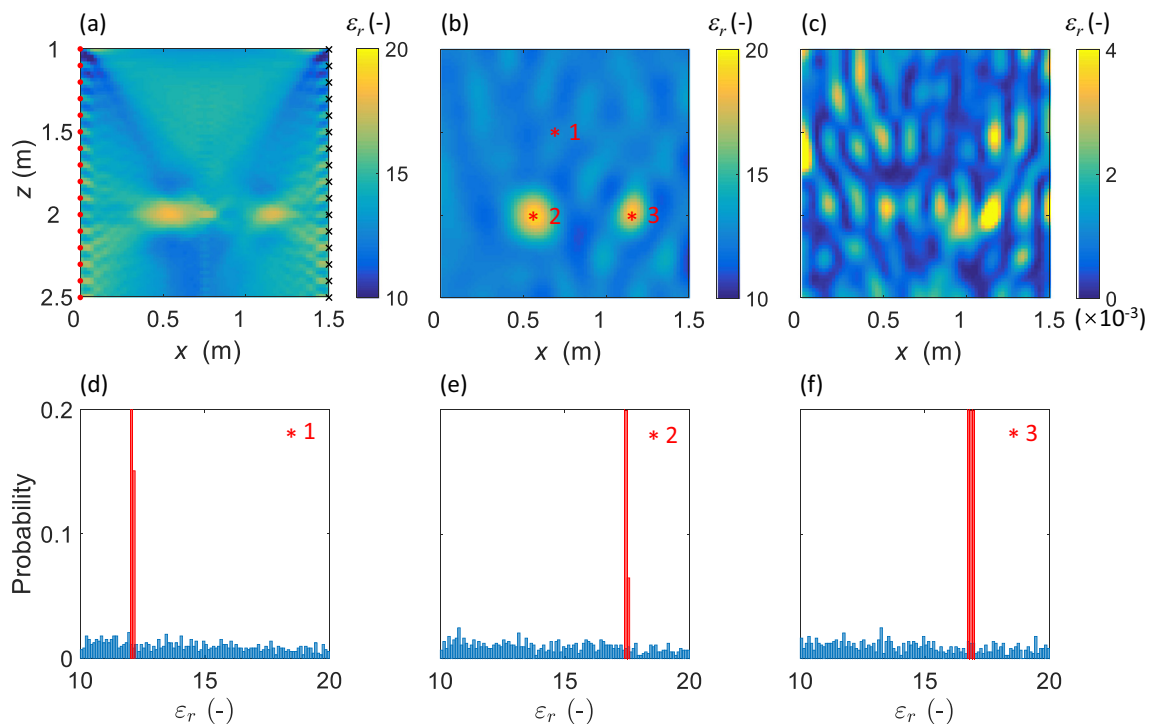

Fig. 4. (a) ε_r field of the concrete diaphragm wall derived from the MOG first-arrival traveltime data using ray tomography, (b) posterior mean ε_r field and (c) the associated variance derived from full-domain inversion with the FDTD-DCT-DREAM$_{(ZS)}$ framework using $d = 196$ DCT-coefficients, and (d)–(f) marginal prior (blue) and posterior (red) histograms of selected parameters at locations 1, 2, and 3 marked with "*" in (b).
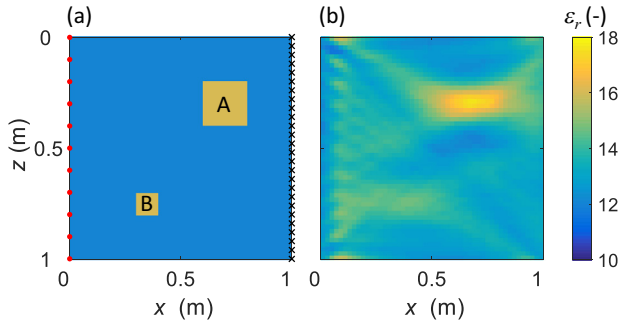
Fig. 5. Case study I: (a) Synthetic ε_r field, and (b) ε_r field derived from ray tomography. The red dots and black crosses mark the vertical positions of the transmitter and receiving antennas, respectively.

0.2 m) and B (0.1 m × 0.1 m), respectively, that consist of a mix of concrete and soil. The relative permittivity of these two structure defects, $\varepsilon_r = 16$, is much higher than the value of $\varepsilon_r = 12$ for the surrounding matrix. We now perform a crosshole GPR experiment using multi-offset profiling with 11 × 26 transmitter-receiver antenna pairs. The antenna setup is depicted graphically in Fig. 5a using 11 equidistant intervals of 0.1 m for the position (red dots) of the transmitter antenna in the left borehole, and 26 equally spaced intervals for the receiver antenna (black crosses) at the right-hand-side of the concrete structure. We implement the 2D-FDTD model developed by Giannopoulos [43] and simulate the crosshole GPR experiment using a grid size of 0.02 m × 0.02 m. The first-arrival traveltimes and waveforms are computed for the 11 × 26 transmitter-antenna pairs. These data are subsequently corrupted with artificial white noise using a measurement error standard deviation equal to 5% of the mean value of all the simulated values. This perturbed data set now serves as our measurement data set, $\widetilde{\mathbf{Y}}$, and is used to back out the relative permittivity field with our two-stage inversion methodology. As the noise level has little impact on the maximum a-posterior (MAP) or posterior mean solution within our FDTD-DCT-DREAM$_{(ZS)}$ framework, it will not be discussed herein. Detailed analysis of the noise effect on the accuracy and reliability of the inversion results can be found in [41].

Before we proceed with our Bayesian inversion methodology, we first present in Fig. 5b the relative permittivity values, ε_r, derived from ray tomography using first-arrival traveltime data and a straight ray-based forward model. This method points out correctly the presence of a structure defect at location A, yet fails to recognize defect B.

We now present the results of the FDTD-DCT-DREAM$_{(ZS)}$ framework of [41] using eight different trials with an increasing number of DCT-coefficients. The FDTD forward model used in all these inversions implements the exact same regular grid of 0.02 m × 0.02 m used previously to create the artificial observations, $\widetilde{\mathbf{Y}}$. If a Cartesian parameterization were used, then a total of 50 × 50 = 2500 values of ε_r need to be estimated to characterize the relative permittivity field of the unit square concrete structure. This equates to one unknown (parameter) for each individual grid cell. Instead, we use the DCT to reduce drastically the dimensionality of the parameter space, and sample the DCT-coefficients in the logarithmic ($\log_{10}$) space using MCMC simulation with the DREAM$_{(ZS)}$ algorithm. We calculate the posterior density of each parameter vector, $\mathbf{m}$, using a bounded Jeffreys' prior [51] equivalent to $p(\mathbf{m}) = \mathcal{U}_d[\log_{10}(10), \log_{10}(18)]$, implement the likelihood function of Eq. (4), and use the same settings of the DREAM$_{(ZS)}$ algorithm as in the field experiment.

Fig. 6 displays the posterior mean ε_r field derived by the FDTD-DCT-DREAM$_{(ZS)}$ framework using (a) 36, (b) 64, (c) 100, (d) 144, (e) 196, (f) 256, (g) 324, and (h) 400 DCT-coefficients. This figure highlights several important findings. In the first place, notice that all eight inversions resolve correctly the relative permittivity of the main matrix of the unit square concrete structure. Note that the inferred permittivity values of

the concrete matrix appear rather similar (smooth fields) for the fewest number of DCT-coefficients, yet exhibit more variability with the use of a larger number of DCT-coefficients. In the second place, all the inversions infer correctly the presence of structure defect A. The spatial resolution of each parameterization is sufficient to warrant inference of this 0.2 × 0.2 m structure defect. In the third place, notice that more than a hundred DCT-coefficients appear necessary to detect the presence of structure defect B. Indeed, this defect is impossible to delineate successfully with a relatively low number of DCT-coefficients, as such parameterizations do not provide the required level of detail and spatial resolution necessary to detect the presence of concrete defects on the order of 0.1 × 0.1 m (or smaller). Finally, the larger the number of DCT-coefficients that is used, the better the shape of both structure defects is resolved, and the better the agreement between the posterior mean ε_r values and their counterparts of the reference field. Indeed, when going from left to right across the bottom panel of Fig. 6 the two structure defects appear sharper and increasingly well resolved and better match their actual shape depicted previously in the reference permittivity field of Fig. 5a. Altogether, these results suggest that the measured waveforms contain sufficient information to warrant an accurate characterization of the relative permittivity field, ε_r, and embedded defects of the unit square concrete structure.

The results presented in Fig. 6 have provided strong support for the intuitive hypothesis that the use of a larger number of DCT-coefficients should enhance the spatial characterization and resolution of the permittivity values, ε_r, of some medium of interest. Indeed, the use of a larger number of DCT-coefficients enhances the level of spatial detail that can be recovered by the inversion, a necessity to recover closely and sharply concrete defects of man-made underground structures. Yet, the pursuit of structure defects poses two important challenges. First, the observed GPR waveform data might not contain enough information to warrant an accurate identification of all of the DCT-coefficients used in the inversion. This is one of the main reasons that we implement a Bayesian approach to characterize properly the uncertainty of the inferred relative permittivity values. Second, the number of DCT-coefficients required to recover structure defects can pose significant computational challenges, as the number of FDTD simulations required by DREAM$_{(ZS)}$ to converge adequately to the posterior distribution, increases rapidly with increasing dimensionality of the parameter space. In Fig. 7a we investigate in more detail the relationship between the number of DCT-coefficients used to characterize the relative permittivity values of the unit square concrete structure and the required computational budget of DREAM$_{(ZS)}$ to approximate the posterior parameter distribution. We also plot in Fig. 7b the evolution of the normalized root-mean-square error (NRMSE)

$$\text{NRMSE} = \frac{1}{(\max\{\widetilde{\mathbf{Y}}\} - \min\{\widetilde{\mathbf{Y}}\})} \sqrt{\frac{1}{T} \sum_{i=1}^{T} (f_i(\mathbf{m}, \widetilde{\mathbf{u}}) - \widetilde{Y}_i)^2} \tag{6}$$

between the posterior mean simulated waveforms corresponding to the relative permittivity fields of Fig. 6 and their observed counterparts, where $\max\{\widetilde{\mathbf{Y}}\}$ and $\min\{\widetilde{\mathbf{Y}}\}$ denote the maximum and minimum value of the measured data, respectively.

We can summarize the main findings as follows. The results in Fig. 7a illustrate that the computational budget required by the FDTD-DCT-DREAM$_{(ZS)}$ framework increases almost linearly with the number of DCT-coefficients used to characterize the relative permittivity field of the unit square concrete structure of interest. Closer inspection of the data points demonstrates that the required CPU-budget approximately doubles with a twofold increase in the number of DCT-coefficients. This linear scaling is an encouraging result, and demonstrates that the DREAM$_{(ZS)}$ algorithm scales well with increasing parameter dimensionality. What is more, the presented data points appear closely aligned around the 1:1 line suggesting that our framework is well designed. The results in Fig. 7b demonstrate that the NRMSE between the N simulated and observed waveforms decreases with the use of a larger
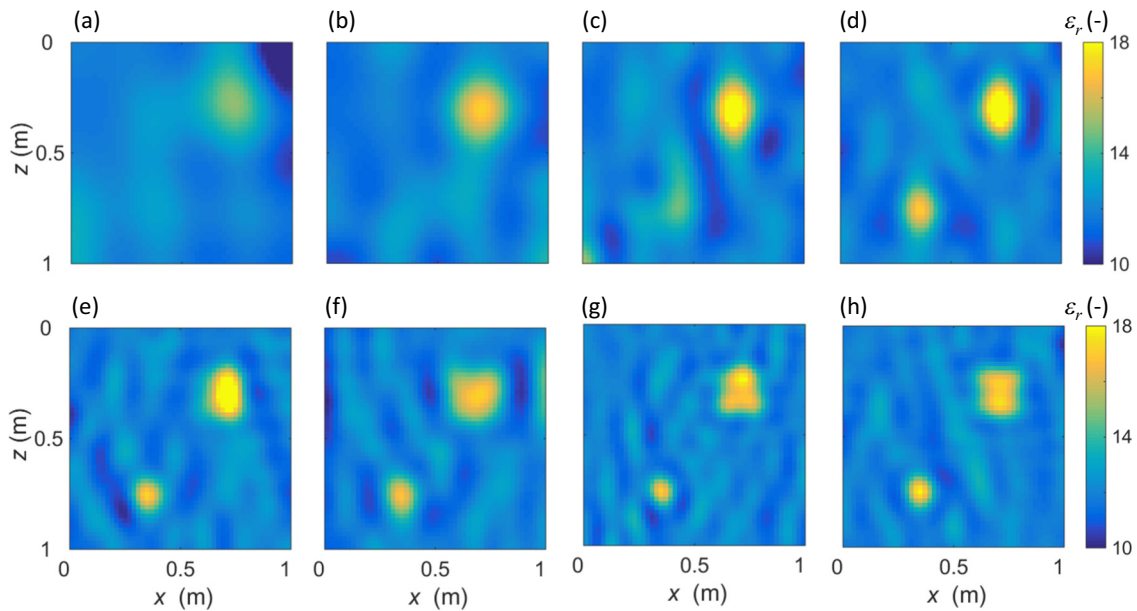
Fig. 6. Case study I: Posterior mean ε_r field derived from full-domain inversion with the FDTD-DCT-DREAM$_{(ZS)}$ framework using (a) 36, (b) 64, (c) 100, (d) 144, (e) 196, (f) 256, (g) 324, and (h) 400 DCT-coefficients.

number of DCT-coefficients. This finding is not surprising and in agreement with the common trade-off found between the goodness of fit of a model and its associated complexity. Indeed, the level of spatial detail that can be recovered by the FDTD-DCT-DREAM$_{(ZS)}$ framework increases with the use of a larger number of DCT-coefficients. This allows the inversion to describe accurately the relative permittivity values of the unit square concrete structure, and delineate sharply the embedded structure defects. This has been demonstrated previously in Fig. 6. Note, however that the benefits of a more complex parameterization decreases rapidly with the number of DCT-coefficients that is used in the inversion. Whereas, the NRMSE decreases from about 0.068 to 0.053 (within-sample) when going from $d = 36$ to $d = 64$ DCT-coefficients, this improvement in the quality of fit is substantially lower between using $d = 324$ and $d = 400$ parameters.

The results presented thus far demonstrate the ability of the FDTD-DCT-DREAM$_{(ZS)}$ to recover successfully the relative permittivity values of the concrete structure. Nevertheless, a substantial number of DCT-coefficients is required to delineate sharply the structure defects (see Fig. 6), at the expense of a relatively large computational effort (see Fig. 7a) required to satisfy the convergence thresholds of the DREAM$_{(ZS)}$ algorithm. This CPU-cost, although affordable with the use of state-of-the-art processors, complicates somewhat practical application of the FDTD-DCT-DREAM$_{(ZS)}$ framework, certainly when this

methodology is used to detect (small) defects in concrete structures whose size extends much beyond the unit square domain used herein. To reduce further the computational requirements of the FDTD-DCT-DREAM$_{(ZS)}$ framework, we now investigate the benefits of a two-stage parametrization approach in which a low-resolution full-domain inversion (first step) is followed by a subsequent inversion (second step) during which the number of DCT-coefficients is enhanced substantially, but limited only to areas of the concrete structure that were shown to exhibit anomalous permittivity values in the first inversion. This approach takes advantage of the fact that only relatively few DCT-coefficients are required to provide a sufficient resolution necessary to characterize adequately the nearly constant relative permittivity values of the concrete matrix. We posit that this two-stage approach should provide an important CPU-time savings compared to the original FDTD-DCT-DREAM$_{(ZS)}$ framework, as spatial detail is restricted only to areas of the concrete structure that have been classified as anomalous.

Fig. 8a presents the results of the first step of our two-stage approach and plots the posterior mean relative permittivity field of the unit square concrete structure derived from full-domain inversion using $d = 144$ DCT-coefficients. This field is identical to the one presented previously in Fig. 6d, and is in good agreement with the synthetic reference field of Fig. 5a. Indeed, the inferred relative permittivity field demonstrates unequivocally the presence of two structure defects
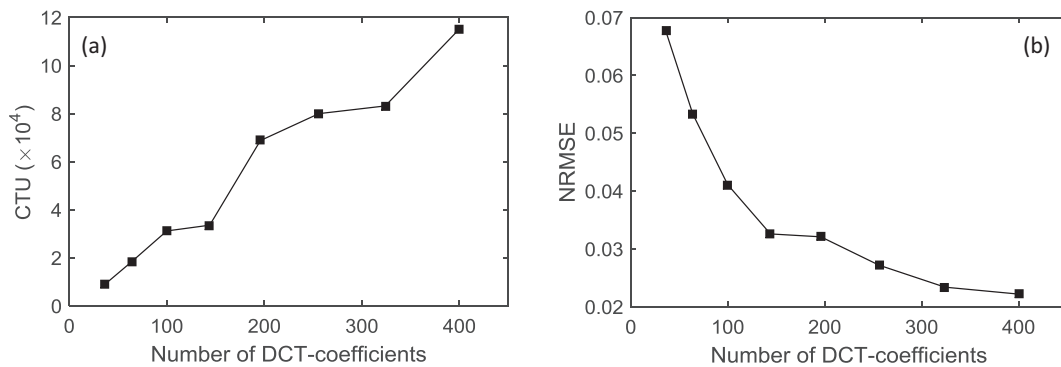

Fig. 7. Case study I: (a) Computational budget required for each DCT-parameterization as measured by the number of CTUs, and (b) Normalized RMSE between the observed and posterior mean simulated GPR waveforms for each model parameterization used herein to characterize the relative permittivity values of the unit square concrete structure.
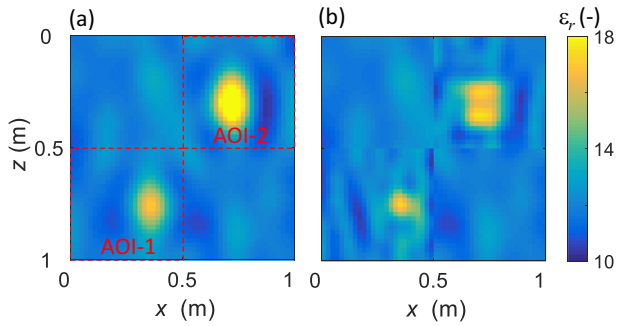
Fig. 8. Case study I: Posterior mean ε_r field derived by (a) full-domain inversion using 144 DCT-coefficients and (b) two-stage inversion using $d = 144$ and $d = 100$ DCT-coefficients for AOI-1 and AOI-2.

(yellow areas) with values of ε_r that are substantially higher than their counterparts of the concrete matrix. Note, however, that the shape of the structure defects is rather poorly resolved as their oval form deviates considerably from their squared counterparts of the reference permittivity field. We therefore investigate these two anomalous areas in more detail and divide the unit square concrete structure in four different pieces of 0.5×0.5 m (see dotted red lines in Fig. 8a) that each are made up of 25×25 grid cells. We now assume posterior mean values of ε_r for the upper-left and bottom-right squares, respectively, and proceed with a second inversion that infers only the relative permittivity values of the remaining two squares, using $d = 144$ and $d = 100$ DCT-coefficients for AOI-1 and AOI-2, respectively. We deliberately use a larger number of DCT-coefficients for AOI-1 as this anomalous area appears noticeably smaller than its counterpart AOI-2, thus requiring a larger spatial resolution to delineate exactly this structure defect.

Fig. 8b presents the results of our second inversion. It is evident that this second inversion has enhanced significantly the spatial resolution of the relative permittivity values in the bottom-left (AOI-1) and top-right (AOI-2) 0.5×0.5 m squares. The two structure defects are easy to recognize with values of the relative permittivity that are much larger than those of the surrounding matrix. The location of the structure defects and their respective ε_r values have hardly changed from the full-domain inversion in step 1. Nonetheless, the second inversion is necessary to delineate exactly both anomalous areas. Indeed, their respective shapes are now in excellent agreement with their counterparts of the reference field.

To provide further insights into the quality of fit, please consider Fig. 9 that presents a comparison between the observed (red dots) and posterior mean simulated waveforms derived from full-domain inversion (solid blue lines) and AOI inversion (solid black lines) using a fixed depth of $z = 0.5$ m of the transmitter antenna and 26 different positions of the receiver antenna. The positions of the receiver antenna are equivalent to the depths of the plotted waveforms. Note that we show only a small portion of the waveform data, large enough to demonstrate the main findings.

The two different inversions exhibit an excellent fit to the observed waveform data. This finding is perhaps not surprising as the stage-1 and stage-2 inversions were shown to both recover the main features of the ε_r reference field of the concrete structure. Some subtle differences between both inversions are difficult to see in the "big" plot, yet appear readily apparent in an enlarged view. Here we present a subplot in the left-hand-side of Fig. 9, which presents a zoomed inset of the waveform in the small black rectangle measured at a receiver antenna depth of 0.44 m (other waveforms have the similar pattern). This subplot demonstrates that the AOI inversion provides the closest fit to the observed GPR waveform data. The enhanced spatial detail of this stage-2 inversion allows the 2D-FDTD model to more accurately track the different features of the measured GPR waveforms.
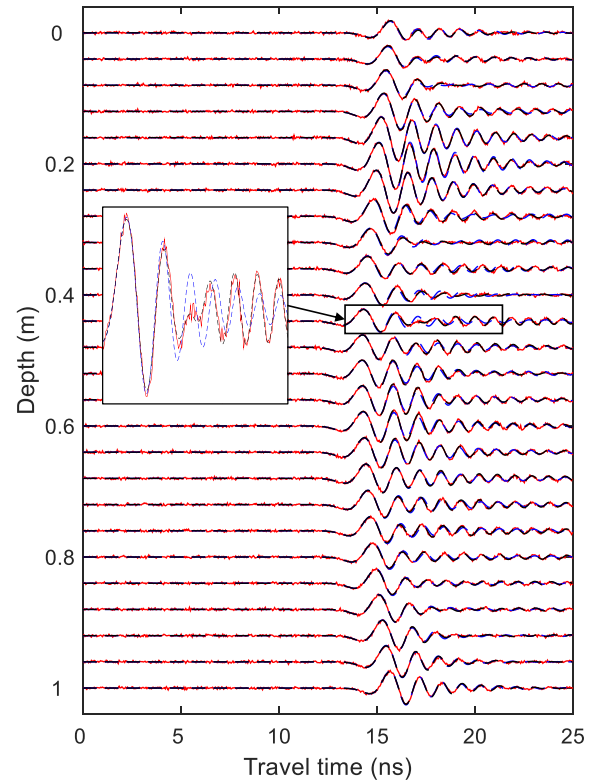

Fig. 9. Case study I: Comparison of the observed (solid red lines) and posterior mean simulated waveforms using full-domain inversion (dotted blue lines), and AOI inversion (dotted black lines) for a fixed depth of the transmitter antenna at $z = 0.5$ m, and 26 different vertical positions of the receiver antenna. These positions of the receiver antenna have been depicted previously in Fig. 5a (black crosses), and correspond exactly to the depths of the plotted waveforms.
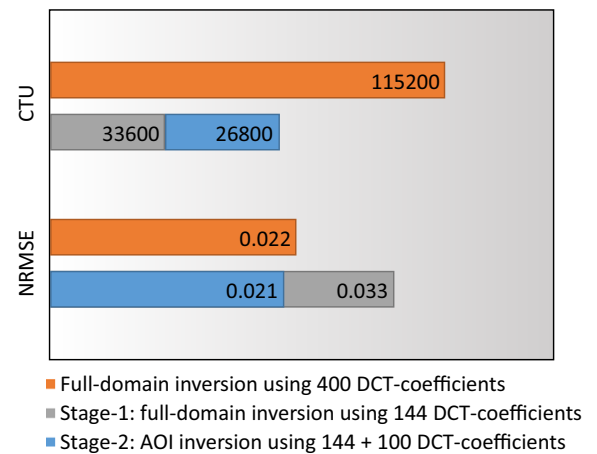

Fig. 10. Case study I: Bar chart which summarizes the computational efficiency (top panel) and goodness of fit (bottom panel) of the FDTD-DCT-DREAM$_{(ZS)}$ framework (in orange) and two-stage inversion approach (gray and blue).

Fig. 10 summarizes in a bar chart the CPU-efficiency of our two-stage inversion approach. This plot presents separately the number of CTUs required by the full-domain (stage-1: $d = 144$) inversion (gray bar) and the AOI (stage-2) inversion (blue bar). For completeness, we also include in the horizontal orange bar the number of CTUs required by the original FDTD-DCT-DREAM$_{(ZS)}$ framework using $d = 400$ DCT-coefficients. This number of DCT-coefficients is required to reach NRMSE values which are approximately similar to those derived from the two-stage inversion approach (see bottom panel). Altogether, the

two bar charts demonstrate that the proposed two-stage inversion approach requires much fewer FDTD model simulations than the FDTD-DCT-DREAM$_{(ZS)}$ framework to reach equivalent results and performance.

The two-stage inversion approach uses more wisely CPU-resources by focusing primarily on those areas of the concrete structure that have been classified as anomalous. This approach sacrifices resolution in the main matrix of the concrete structure, in lieu of a much more detailed characterization of the aberrant permittivity areas. We can quantify the spatial resolution that is used to back out the structure defects by looking at the number of DCT-coefficients that is used in each anomalous permittivity area. The higher this ratio is, the more features (spatial detail) can be recovered. The original FDTD-DCT-DREAM$_{(ZS)}$ framework uses $d = 400$ DCT-coefficients to characterize the relative permittivity values of 2500 grid cells, that is, an average of 0.16 DCT-coefficient per grid cell. The second inversion used in our two-stage approach uses a total of $d = 144$ and $d = 100$ DCT-coefficients to describe the relative permittivity values of AOI-1 and AOI-2, respectively. These two areas of 0.5×0.5 m are each made up of 625 grid cells. This results in a ratio of about 0.23 and 0.16 DCT-coefficient per individual grid cell of AOI-1 and AOI-2, respectively. These listed ratios support the use of a two-stage inversion approach and explain the different findings of this case study.

4.2. Case study II: field experiment

We now evaluate the merits of our two-stage inversion approach by application to MOG waveform data measured by crosshole GPR in the field experiment described in the previous section.

Fig. 11a presents the results of the first step of our two-stage approach and plots the posterior mean relative permittivity field of the front panel of the experimental structure derived from full-domain inversion using $d = 144$ DCT-coefficients. It is evident that this field has a lower spatial resolution than its counterpart of $d = 196$ DCT-coefficients (see Fig. 4b), yet the level of detail of the image is sufficient to expose the two structure defects. Note that this inversion requires only 78,400 CTUs to satisfy the convergence thresholds of the 144 DCT-coefficients, which is less than half the computational budget of 164,000 CTUs required for $d = 196$ DCT-coefficients.

To further refine our results, we define two AOIs of size 0.54 m × 0.54 m (AOI-1) and 0.4 m × 0.4 m (AOI-2), respectively (see Fig. 11a), and proceed with our AOI inversion approach (step-2). We use $d = 144$ and $d = 100$ DCT-coefficients to characterize the ε_r values of both areas - which equates to the use of about 0.20 and 0.25 DCT-coefficients per individual grid cell of AOI-1 and AOI-2, respectively. This ratio is much larger than that used by the full-domain FDTD-DCT-DREAM$_{(ZS)}$ framework (which is 0.03), and enhances considerably the spatial detail that can be resolved within each anomalous area. About 60,000 CTUs
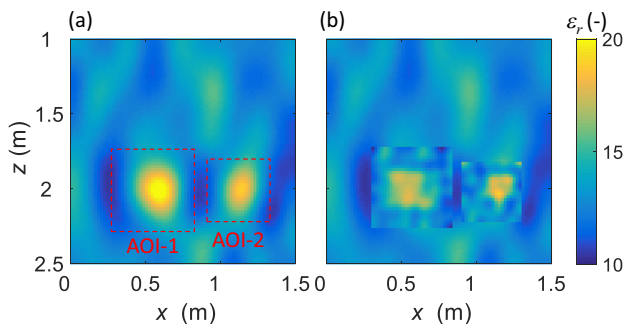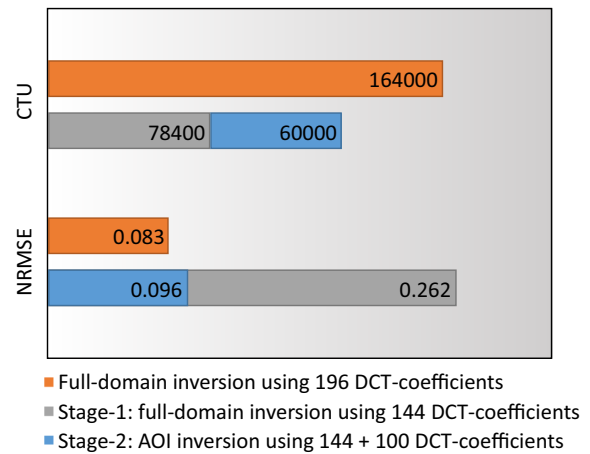

Fig. 12. Case study II: Bar chart which summarizes the computational efficiency (top panel) and goodness of fit (bottom panel) of the full-domain FDTD-DCT-DREAM$_{(ZS)}$ framework (in orange) and two-stage inversion approach (gray and blue).

are required for this second-stage inversion to reach convergence to the posterior distribution of the DCT-coefficients. The total computational effort of two-stage inversion thus equates to $78,400 + 60,000 = 138,400$ CTUs. Both defects now appear sharply demarcated and their features (size and shape) well resolved and in good agreement with the features of the two defects (A and B) in the concrete wall (see Fig. 11b). This enhanced characterization of the relative permittivity field reduces the NRMSE between the observed and posterior mean simulated waveforms from 0.262 to 0.096. These findings are encouraging and supports practical application of our two-stage inversion method.

We now turn our attention to the computational budget and goodness of fit of the original FDTD-DCT-DREAM$_{(ZS)}$ framework and our two-stage inversion approach. Fig. 12 summarizes in a bar chart the CPU-efficiency of our two-stage inversion approach. This plot presents separately the number of CTUs required by the first-stage full-domain inversion using $d = 144$ DCT-coefficients (gray bar), and the second-stage AOI inversion using $d = 144 + 100$ DCT-coefficients (blue bar). This number is 15% less than the number of CTUs required by the original FDTD-DCT-DREAM$_{(ZS)}$ framework using $d = 196$ DCT-coefficients (orange bar). Meanwhile, the two-stage inversion approach reaches a slightly higher NRMSE value than that derived from the original FDTD-DCT-DREAM$_{(ZS)}$ framework (see bottom panel). Nevertheless, the two-stage inversion approach still resolves better spatial details (see Fig. 11b). Altogether, the proposed two-stage inversion approach requires much fewer FDTD model simulations than the FDTD-DCT-DREAM$_{(ZS)}$ framework to reach equivalent results and performance.

5. Summary and conclusion

In a recent paper by [41] we have developed a Bayesian inversion method of crosshole GPR experiments on man-made underground structures to guide detection of concrete defects. This method uses as main building blocks two-dimensional finite-difference time-domain solution of the Maxwell's equations, the discrete cosine transform, and MCMC simulation with the DREAM$_{(ZS)}$ algorithm to explore rapidly and efficiently the posterior distribution of the relatively permittivity field of the concrete structure of interest. The usefulness and applicability of the FDTD-DCT-DREAM$_{(ZS)}$ framework was demonstrated on synthetic test examples involving a unit square underground structure with different defects. In this paper, we evaluated further the merits of this method using measured waveform data from a crosshole GPR-experiment of a diaphragm wall model. The two structure defects in this wall were successfully resolved by the FDTD-DCT-DREAM$_{(ZS)}$ framework.

Fig. 11. Case study II: Posterior mean ε_r fields derived by two-stage inversion using the MOG waveform data. (a) Stage-1: full-domain inversion using $d = 144$ DCT-coefficients, and (b) stage-2: AOI inversion using $d = 144$ and $d = 100$ DCT-coefficients for AOI-1 and AOI-2, respectively.

The results of this real-world case study reiterated the relatively large computational resources required by FDTD-DCT-DREAM$_{(ZS)}$ framework to solve for the dielectric properties of the diaphragm wall. Almost all of these resources are consumed by the repeated numerical solution of Maxwell's equations necessary to extract the wall's relative permittivity field from the measured waveform data. Of course, we can speed-up our framework by using fewer DCT-coefficients, but this approach sacrifices spatial resolution and may not expose sufficiently structure defects, particularly if these anomalous areas appear relatively small in comparison to the surrounding structure. We therefore introduced herein a two-stage inversion method to help delineate, at reduced CPU-cost, the exact location and shape of small structure defects. Herein, a low-resolution inversion composed of relatively few DCT-coefficients (stage-1) is used to determine roughly the presence of structure defects, followed by a second inversion (stage-2) with much enhanced resolution in those areas with anomalous (suspicious) permittivity values. This two-stage inversion approach uses more wisely CPU-resources by focusing primarily on those areas of the concrete structure that have been classified as anomalous. This approach sacrifices resolution in the main matrix of the concrete structure, in lieu of a much more detailed characterization of the aberrant permittivity areas.

We illustrated the benefits of this two-stage inversion approach using artificial waveform data from a synthetic GPR-experiment on a unit square concrete body with two embedded structure defects, and the measured waveform data of the diaphragm wall. Our results demonstrate that the proposed two-stage inversion method recovers successfully the location and shape of structure defects, at a computational cost that is considerably lower than the original FDTD-DCT-DREAM$_{(ZS)}$ framework.

Acknowledgments

References

[1] G. Grandjean, J.C. Gourry, A. Bitri, Evaluation of GPR techniques for civil-engineering applications: study on a test site, J. Appl. Geophys. 45 (3) (2000) 141–156, https://doi.org/10.1016/S0926-9851(00)00021-5.

[2] F. Zhang, X. Xie, H. Huang, Application of ground penetrating radar in grouting evaluation for shield tunnel construction, Tunn. Undergr. Space Technol. 25 (2) (2010) 99–107, https://doi.org/10.1016/j.tust.2009.09.006.

[3] M. Solla, H. Lorenzo, F.I. Rial, A. Novo, Ground-penetrating radar for the structural evaluation of masonry bridges: results and interpretational tools, Constr. Build. Mater. 29 (2012) 458–465, https://doi.org/10.1016/j.conbuildmat.2011.10.001.

[4] S. Demircia, E. Yigitb, I.H. Eskidemirc, C. Ozdemira, Ground penetrating radar imaging of water leaks from buried pipes based on back-projection method, NDT&E Int. 47 (2012) 35–42, https://doi.org/10.1016/j.ndteint.2011.12.008.

[5] A. Kalogeropoulos, J. van der Kruk, J. Hugenschmidt, J. Bikowski, E. Bruhwiler, Full-waveform GPR inversion to assess chloride gradients in concrete, NDT&E Int. 57 (2013) 74–84, https://doi.org/10.1016/j.ndteint.2013.03.003.

[6] M. Korff, R.J. Mair, A.F. van Tol, F. Kaalberg, Building damage and repair due to leakage in a deep excavation, Proc. Inst. Civ. Eng. - Forensic Eng. 164 (4) (2011) 165–177, https://doi.org/10.1680/feng.2011.164.4.165.

[7] D.A. Noon, G.F. Stickley, D. Longstaff, A frequency-independent characterisation of GPR penetration and resolution performance, J. Appl. Geophys. 40 (1-3) (1998) 127–137, https://doi.org/10.1016/S0926-9851(98)00008-1.

[8] E. Slob, M. Sato, G. Olhoeft, Surface and borehole ground-penetrating-radar developments, Geophysics 75 (5) (2010) 75A103–175A120, https://doi.org/10.1190/1.3480619.

[9] H. Qin, X. Xie, Design and test of an improved dipole antenna for detecting enclosure structure defects by cross-hole GPR, IEEE J. Sel. Top. Appl. Earth Obs. Remote Sens. 9 (1) (2016) 108–114, https://doi.org/10.1109/JSTARS.2015.2466450.

[10] M.N. Soutsos, J.H. Bungey, S.G. Millard, M.R. Shaw, A. Patterson, Dielectric properties of concrete and their influence on radar testing, NDT & E Int. 34 (6) (2001) 419–425, https://doi.org/10.1016/S0963-8695(01)00009-3.

[11] G. Klysz, J.P. Balayssac, Determination of volumetric water content of concrete using ground-penetrating radar, Cem. Concr. Res. 37 (8) (2007) 1164–1171, https://doi.org/10.1016/j.cemconres.2007.04.010.

[12] A. Louis, A. van der Wielen, L. Courard, F. Nguyen, GPR detection of saturated areas into concrete in the presence of a water gradient, Proceedings of the 14th International Conference on Ground Penetrating Radar (GPR), IEEE, Shanghai, China, 2012, pp. 473–478, https://doi.org/10.1109/ICGPR.2012.6254912.

[13] A.J. Witten, J.E. Molyneux, J.E. Nyquist, Ground penetrating radar tomography: algorithms and case studies, IEEE Trans. Geosci. Remote Sens. 32 (2) (1994) 461–467, https://doi.org/10.1109/36.295060.

[14] J.E. Molyneux, Ground penetrating radar tomography, Proceedings of the International Conference on Acoustics, Speech, and Signal Processing, IEEE, Detroit, MI, USA, 1995, pp. 2813–2816, https://doi.org/10.1109/ICASSP.1995.479430.

[15] K.A. Dines, R.J. Lytle, Computerized geophysical tomography, Proc. IEEE 67 (7) (1979) 1065–1073, https://doi.org/10.1109/PROC.1979.11390.

[16] S. Hanafy, S.A. al Hagrey, Ground-penetrating radar tomography for soil-moisture heterogeneity, Geophysics 71 (1) (2006) K9–K18, https://doi.org/10.1190/1.2159052.

[17] C. Balkaya, Z. Akcig, G. Gokturkler, A comparison of two travel-time tomography schemes for crosshole radar data: Eikonal-equation-based inversion versus ray-based inversion, J. Environ. Eng. Geophys. 15 (4) (2010) 203–218, https://doi.org/10.2113/JEEG15.4.203.

[18] P.Y. Chang, D. Alumbaugh, An analysis of the cross-borehole GPR tomography for imaging the development of the infiltrated fluid plume, J. Geophys. Eng. 8 (2) (2011) 294–307, https://doi.org/10.1088/1742-2132/8/2/014.

[19] P.R. Williamson, M.H. Worthington, Resolution limits in ray tomography due to wave behavior: numerical experiments, Geophysics 58 (5) (1993) 727–735, https://doi.org/10.1190/1.1443457.

[20] M.L. Buursink, T.C. Johnson, P.S. Routh, M.D. Knoll, Crosshole radar velocity tomography with finite-frequency Fresnel volume sensitivities, Geophys. J. Int. 172 (1) (2008) 1–17, https://doi.org/10.1111/j.1365-246X.2007.03589.x.

[21] J.R. Ernst, H. Maurer, A.G. Green, K. Holliger, Full-waveform inversion of crosshole radar data based on 2-D finite-difference time-domain solutions of Maxwell's equations, IEEE Trans. Geosci. Remote Sens. 45 (9) (2007) 2807–2828, https://doi.org/10.1109/tgrs.2007.901048.

[22] J.R. Ernst, A.G. Green, H. Maurer, K. Holliger, Application of a new 2D time-domain full-waveform inversion scheme to crosshole radar data, Geophysics 72 (5) (2007) J53–J64, https://doi.org/10.1190/1.2761848.

[23] G.A. Meles, J. van der Kruk, S.A. Greenhalgh, J.R. Ernst, H. Maurer, A.G. Green, A new vector waveform inversion algorithm for simultaneous updating of conductivity and permittivity parameters from combination crosshole/borehole-to-surface GPR data, IEEE Trans. Geosci. Remote Sens. 48 (9) (2010) 3391–3407, https://doi.org/10.1109/TGRS.2010.2046670.

[24] A. Klotzsche, J. van der Kruk, G.A. Meles, J. Doetsch, H. Maurer, N. Linde, Full-waveform inversion of cross-hole ground-penetrating radar data to characterize a gravel aquifer close to the Thur River, Switzerland, Near Surf. Geophys. 8 (6) (2010) 635–649, https://doi.org/10.3997/1873-0604.2010054.

[25] J.H. Kim, T. Kobayashi, S.K. Lee, Admittance inversion of crosshole radar data, Proceedings of the 13th International Conference on Ground Penetrating Radar (GPR), IEEE, Lecce, Italy, 2010, pp. 1–6, https://doi.org/10.1109/ICGPR.2010.5550162.

[26] M. El Bouajaji, S. Lanteri, M. Yedlin, Discontinuous Galerkin frequency domain forward modelling for the inversion of electric permittivity in the 2D case, Geophys. Prospect. 59 (5) (2011) 920–933, https://doi.org/10.1111/j.1365-2478.2011.00973.x.

[27] K.J. Ellefsen, A.T. Mazzella, R.J. Horton, J.R. McKenna, Phase and amplitude inversion of crosswell radar data, Geophysics 76 (3) (2011) J1–J12, https://doi.org/10.1190/1.3554412.

[28] G.A. Meles, S.A. Greenhalgh, A.G. Green, H. Maurer, J. van der Kruk, GPR full-waveform sensitivity and resolution analysis using an FDTD adjoint method, IEEE Trans. Geosci. Remote Sens. 50 (5) (2012) 1881–1896, https://doi.org/10.1109/TGRS.2011.2170078.

[29] G. Meles, S. Greenhalgh, J. van der Kruk, A. Green, H. Maurer, Taming the non-linearity problem in GPR full-waveform inversion for high contrast media, J. Appl. Geophys. 78 (2012) 31–43, https://doi.org/10.1016/j.jappgeo.2011.12.001.

[30] X. Yang, A. Klotzsche, G. Meles, H. Vereecken, J. van der Kruk, Improvements in crosshole GPR full-waveform inversion and application on data measured at the Boise Hydrogeophysics Research Site, J. Appl. Geophys. 99 (2013) 114–124, https://doi.org/10.1016/j.jappgeo.2013.08.007.

[31] M. Oberrohrmann, A. Klotzsche, H. Vereecken, J. van der Kruk, Optimization of acquisition setup for cross-hole GPR full-waveform inversion using checkerboard analysis, Near Surface Geophysics 11 (2) (2013) 197–209, https://doi.org/10.3997/1873-0604.2012045.

[32] E. Slob, Uncertainty in ground penetrating radar models, Proceedings of the 13th International Conference on Ground Penetrating Radar (GPR), IEEE, Lecce, Italy, 2010, pp. 1–5, https://doi.org/10.1109/ICGPR.2010.5550154.

[33] J. Irving, K. Singha, Stochastic inversion of tracer test and electrical geophysical data to estimate hydraulic conductivities, Water Resour. Res. 46 (11) (2010) W11514, https://doi.org/10.1029/2009WR008340.

[34] K.S. Cordua, T.M. Hansen, K. Mosegaard, Monte Carlo full-waveform inversion of crosshole GPR data using multiple-point geostatistical a priori information, Geophysics 77 (2) (2012) H19–H31, https://doi.org/10.1190/GEO2011-0170.1.

[35] B. Dafflon, W. Barrash, Three-dimensional stochastic estimation of porosity distribution: benefits of using ground-penetrating radar velocity tomograms in simulated-annealing-based or Bayesian sequential simulation approaches, Water Resour. Res. 48 (5) (2012) W05553, https://doi.org/10.1029/2011WR010916.

[36] J. Bikowski, J.A. Huisman, J.A. Vrugt, H. Vereecken, J. van der Kruk, Integrated analysis of waveguide dispersed GPR pulses using deterministic and Bayesian inversion methods, Near Surface Geophys. 10 (6) (2012) 641–652, https://doi.org/

10.3997/1873-0604.2012041.

[37] M. Scholer, J. Irving, M.C. Looms, L. Nielsen, K. Holliger, Bayesian Markov-chain-Monte-Carlo inversion of time-lapse crosshole GPR data to characterize the vadose zone at the Arrenaes Site, Denmark, Vadose Zone J. 11 (4) (2012), https://doi.org/10.2136/vzj2011.0153.

[38] E. Laloy, N. Linde, J.A. Vrugt, Mass conservative three-dimensional water tracer distribution from Markov chain Monte Carlo inversion of time-lapse ground-penetrating radar data, Water Resour. Res. 48 (7) (2012) W07510, https://doi.org/10.1029/2011wr011238.

[39] N. Linde, J.A. Vrugt, Distributed soil moisture from crosshole ground-penetrating radar travel times using stochastic inversion, Vadose Zone J. 12 (1) (2013), https://doi.org/10.2136/vzj2012.0101.

[40] T. Lochbuhler, J.A. Vrugt, M. Sadegh, N. Linde, Summary statistics from training images as prior information in probabilistic inversion, Geophys. J. Int. 201 (1) (2015) 157–171, https://doi.org/10.1093/gji/ggv008.

[41] H. Qin, X. Xie, J.A. Vrugt, K. Zeng, G. Hong, Underground structure defect detection and reconstruction using crosshole GPR and Bayesian waveform inversion, Autom. Constr. 68 (2016) 156–169, https://doi.org/10.1016/j.autcon.2016.03.011.

[42] K.S. Yee, Numerical solution of initial boundary value problems involving Maxwell's equations in isotropic media, IEEE Trans. Antennas Propag. 14 (3) (1966) 302–307, https://doi.org/10.1109/TAP.1966.1138693.

[43] A. Giannopoulos, Modelling ground penetrating radar by GprMax, Constr. Build. Mater. 19 (10) (2005) 755–762, https://doi.org/10.1016/j.conbuildmat.2005.06.007.

[44] N. Ahmed, T. Natarajan, K.R. Rao, Discrete cosine transform, IEEE Trans. Comput. C-23 (1) (1974) 90–93, https://doi.org/10.1109/T-C.1974.223784.

[45] B. Jafarpour, V.K. Goyal, D.B. McLaughlin, W.T. Freeman, Transform-domain sparsity regularization for inverse problems in geosciences, Geophysics 74 (5) (2009) R69–R83, https://doi.org/10.1190/1.3157250.

[46] C.J.F. ter Braak, A Markov chain Monte Carlo version of the genetic algorithm differential evolution: easy Bayesian computing for real parameter spaces, Stat. Comput. 16 (3) (2006) 239–249, https://doi.org/10.1007/s11222-006-8769-1.

[47] C.J.F. ter Braak, J.A. Vrugt, Differential evolution Markov chain with snooker updater and fewer chains, Stat. Comput. 18 (4) (2008) 435–446, https://doi.org/10.1007/s11222-008-9104-9.

[48] J.A. Vrugt, C.J.F. ter Braak, C.G.H. Diks, B.A. Robinson, J.M. Hyman, D. Higdon, Accelerating Markov chain Monte Carlo simulation by differential evolution with self-adaptive randomized subspace sampling, Int. J. Nonlinear Sci. Numer. Simul. 10 (3) (2009) 273–290, https://doi.org/10.1515/IJNSNS.2009.10.3.273.

[49] J.A. Vrugt, Markov chain Monte Carlo simulation using the DREAM software package: theory, concepts, and MATLAB implementation, Environ. Model Softw. 75 (2016) 273–316, https://doi.org/10.1016/j.envsoft.2015.08.013.

[50] X. Xie, H. Qin, G. Hong, Y. Chen, K. Zeng, Crosshole radar for underground structure defect detection: system design and model experiment, Proceedings of the 16th International Conference on Ground Penetrating Radar (GPR), IEEE, Hong Kong, China, 2016, pp. 1–5, https://doi.org/10.1109/ICGPR.2016.7572618.

[51] H. Jeffreys, An invariant form for the prior probability in estimation problems, Proc. R. Soc. Lond. A: Math. Phys. Eng. Sci. 186 (1007) (1946) 453–461, https://doi.org/10.1098/rspa.1946.0056.

[52] A. Gelman, D.B. Rubin, Inference from iterative simulation using multiple sequences, Stat. Sci. 7 (4) (1992) 457–472, https://doi.org/10.1214/ss/1177011136.